

On the climbing ability of passively suspended tracked robots

Giulio Reina

Professor

Department of Mechanics,
Mathematics, and Management
Polytechnic University of Bari
via Orabona 4, 70126 Bari, Italy
Email: giulio.reina@poliba.it

Giacomo Mantriota

Professor

Department of Mechanics,
Mathematics, and Management
Polytechnic University of Bari
via Orabona 4, 70126 Bari, Italy
Email: giacomo.mantriota@poliba.it

ABSTRACT

This paper investigates the obstacle-climbing ability of a novel passively articulated robot, Polibot, which is compared to a standard tracked robot using a fixed wheel configuration. Two test cases are analysed: the traverse of a single obstacle and the navigation upward along a vertical surface. Both scenarios are analytically solved using a quasi-static Newton-Euler approach. The dynamic equilibrium of the system is also defined using an energetic approach, focusing on the energy loss from the wheel-ground slippage. Understanding the role played by the different energy components contributes to shedding light on the fundamental mechanisms underlying the negotiation of obstacles and highly challenging terrain, in general, by suspended tracked robots. Finally, experimental results are presented to validate the proposed approach in real-world conditions.

1 Introduction

The use of rough-terrain mobile robots has been demonstrated in diverse fields, including space exploration [1], precision agriculture [2], search and rescue operations [3], automation [4], and maintenance [5]. Based on the design requirements of the application in terms of operating speed, efficiency, and mobility, the best locomotion type can be chosen. The most common solutions are wheeled, legged, tracked, or hybrid. Tracked robots are known to excel in traction efficiency [6], especially on loose soil [7], and obstacle negotiation [8]. Nevertheless, in cases where the terrain exhibits significant curvature (i.e., when the track size is relatively larger than the terrain irregularity), only a portion of the track can come into contact with the ground, which hampers the ability of a robot to traverse rough terrain. Various articulated tracks have been proposed to overcome this limitation with the idea of replacing a long track with a combination of short tracks that can be controlled to achieve stable contact in rough terrain, such as Chaos [9], Kenaf [10] and iRobot's Packbot [11]. However, the previously mentioned mobile robots have actively articulated tracks that require additional hardware and complex control strategy. In the last few years, an increasing interest has been given to new locomotion mechanisms with passively suspended tracks, which automatically adapt to the terrain shape [12]. In [13], an example is given in which a robot is equipped with separate driving tracks at each of its four corners. These tracks are connected with the main body through two rocker links and four pitch-roll passive joints with two degrees of freedom. In [14] a passive bioinspired suspension is discussed to address the trade-off issue between load capacity and vibration isolation. In other research related to wheeled robots, the kinetostatic modeling of a passive articulated suspension for planetary rovers has been presented [15].

Recently, the authors presented Polibot, a new passively suspended tracked robot that can be employed in search-and-rescue operations, agriculture, or planetary exploration. Polibot is shown in Figure 1 as operating in a commercial farm.

20 Typically, in the design of tracked robots, the axes of rotation of the ground wheels are fixed to the chassis. In contrast,
 21 suspended solutions allow the ground wheels to move up and down with respect to each other. In the case of Polibot, an
 22 articulated suspension system is adopted, in which the chassis is connected to each of the four ground wheels through swing
 23 arms, resembling the legs of a multi-legged insect. The design, set-up, and analytical modeling of the robot were discussed
 24 in [16], whereas its multibody digital twin was developed in [17]. The novel contributions of this research are multiple.
 25 The obstacle climbing performance of Polibot is investigated in terms of the minimum requirement of friction coefficient
 26 and drive torque, and change in the distribution of vertical forces using a quasi-static Newton-Euler model for the two cases
 27 of the traverse of a single obstacle and the upward navigation of a wall. As a comparative benchmark, the results have
 28 been contrasted with those obtained from a standard tracked analog with fixed wheels. The behavior of Polibot is also
 29 analytically solved using the principle of virtual work, highlighting the role played by the different energy types involved.
 30 Special attention is given to the elastic potential energy stored in the robot suspension and to the energy loss due to wheel-
 31 ground slippage. These aspects are seldom addressed in the literature and their understanding contributes to shed light on the
 32 fundamental mechanisms underlying the negotiation of irregular terrain. Finally, experimental results are presented obtained
 33 from the real robot in terms of required drive torque that confirm the theoretical approach.

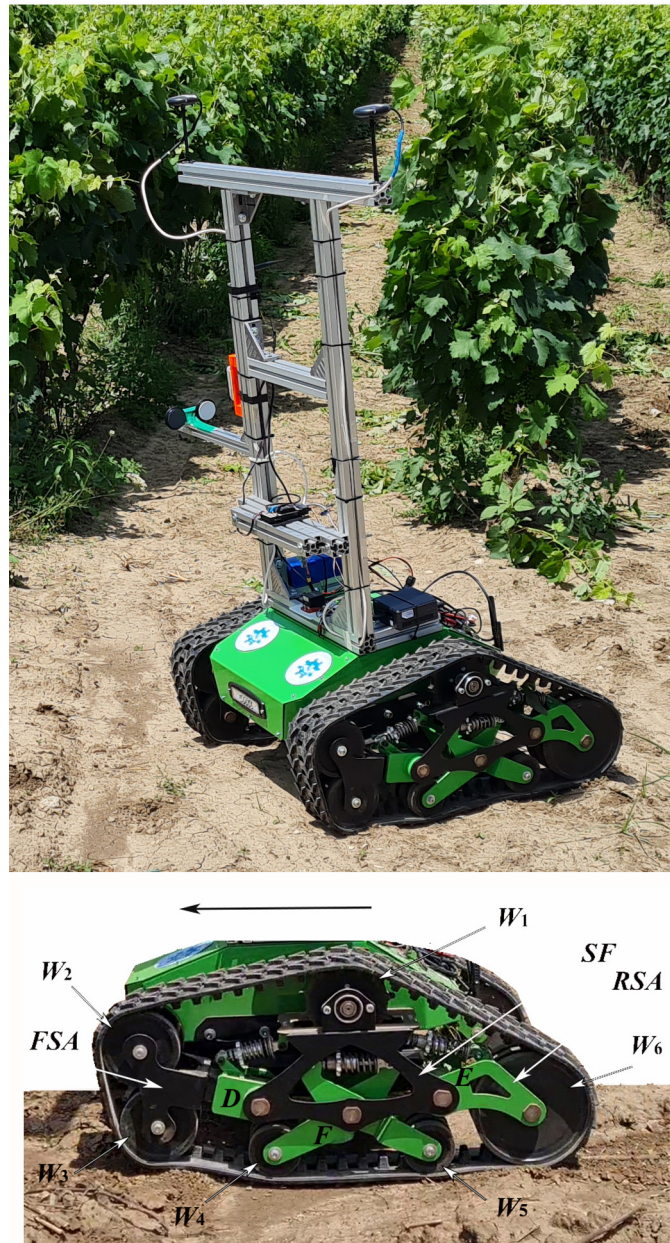


Fig. 1: Polibot: an example of a passively suspended tracked robot; (top) the robot operating in a vineyard, (bottom) details of the suspension system

34 The paper is organized as follows. A brief description of Polibot and its main features is provided in Section 2. Section
 35 3 details the analytical model developed to assess the obstacle climbing ability. Numeric results are presented and discussed
 36 in Section 4. Section 5 presents the experimental results obtained from the Polibot robot operating in real conditions. Finally,
 37 Section 6 draws the relevant conclusions and closes the paper.

38 2 The passively suspended Polibot

39 A close-up of the articulated track suspension system adopted by Polibot is shown in the lower part of Figure 1. The
 40 four ground wheels, W_i ($i = 3, \dots, 6$), can move independently with respect to the triangle-shaped frame SF that is part of
 41 the robot chassis, providing remarkable adaptability to the shape of the terrain. This is achieved by using swing arms, whose
 42 rotation is controlled by spring-damper elements. The front swing arm (FSA) and the rear swing arm (RSA) allow wheels
 43 3 and 6 to rotate around the hinges D and E , respectively. The central bogie-like structure allows wheels 4 and 5 to rotate
 44 around the hinge F . Beyond the ground wheels, the rubber track reinforced with steel cables envelopes the sprocket W_1 and
 45 the idler W_2 .

46 Polibot has a net weight of approximately 70 kg with a payload up to 40 kg and covers an overall supporting area of 1.5×1
 47 m. It is powered by two 350 W and 24 VDC brushed motors and turns by skid-steering. With a maximum speed of 2 m/s,
 48 Polibot can survey one vineyard hectare in about 40 minutes. The use of 1.5×0.1 m tracks ensures a ground pressure of 7
 49 kPa at the maximum payload that is much lower than the agronomic damage threshold (≈ 40 kPa).

50 3 Obstacle climbing ability

51 For rough-terrain robots, the ability to overcome rocks is of primary importance. Referring to Fig. 2, one single rock
 52 can be modeled as a step-like obstacle, which is a conservative assumption. The contact point depends on the geometry of
 53 the obstacle and can be defined by referring to the wheel-terrain contact plane, as detailed in [18]. As an example, the contact
 54 model for the front Wheel 3 that crosses the obstacle is shown in Fig. 3. It is assumed that a contact force between the wheel
 55 and the ground, $C_3 = [F_3, N_3]^T$, exists at the point CP_3 . The tension acting on the upper and lower branches of the track
 56 is indicated, respectively, as T_1 and T_2 . The angle α_3 measures the inclination between the wheel-terrain contact plane and the
 57 horizontal direction. Figure 3 shows the change in the vertical displacement of Wheel 3, Δz_3 , as a function of the contact
 58 angle α_3 (note that the complementary angle of α_3 is actually considered in the graph), during the entire obstacle negotiation
 59 maneuver. The relationship between Δz_3 and α_3 can be obtained analytically as:

$$\Delta z_3 = R \left(\cos \alpha_3 - 1 + \frac{h}{R} \right) \quad (1)$$

60 being h the obstacle height and R the wheel radius.

61 3.1 Robot modeling

62 This section briefly recalls the half-symmetry model that describes the inverse kinematics of Polibot, as previously
 63 developed by the authors. The interested readers are referred to [16] for more details. Being underconstrained, the problem
 64 can be solved by coupling the inverse kinematics with the quasi-static equilibrium of the system to include the elastic
 65 deformations of the suspension, leading to the following compact matrix form of the force distribution equation:

$$G_c \cdot f_c + G_{int} \cdot f_{int} = f_s \quad (2)$$

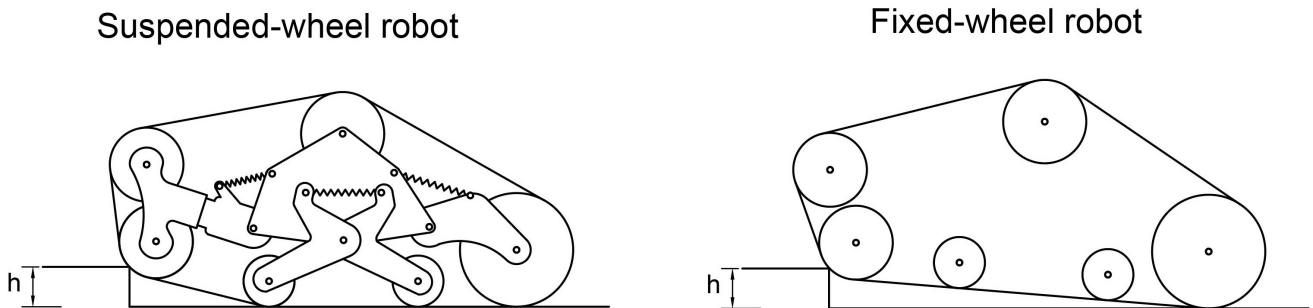


Fig. 2: Obstacle negotiation for a suspended (left) and fixed-wheel (right) tracked robot.

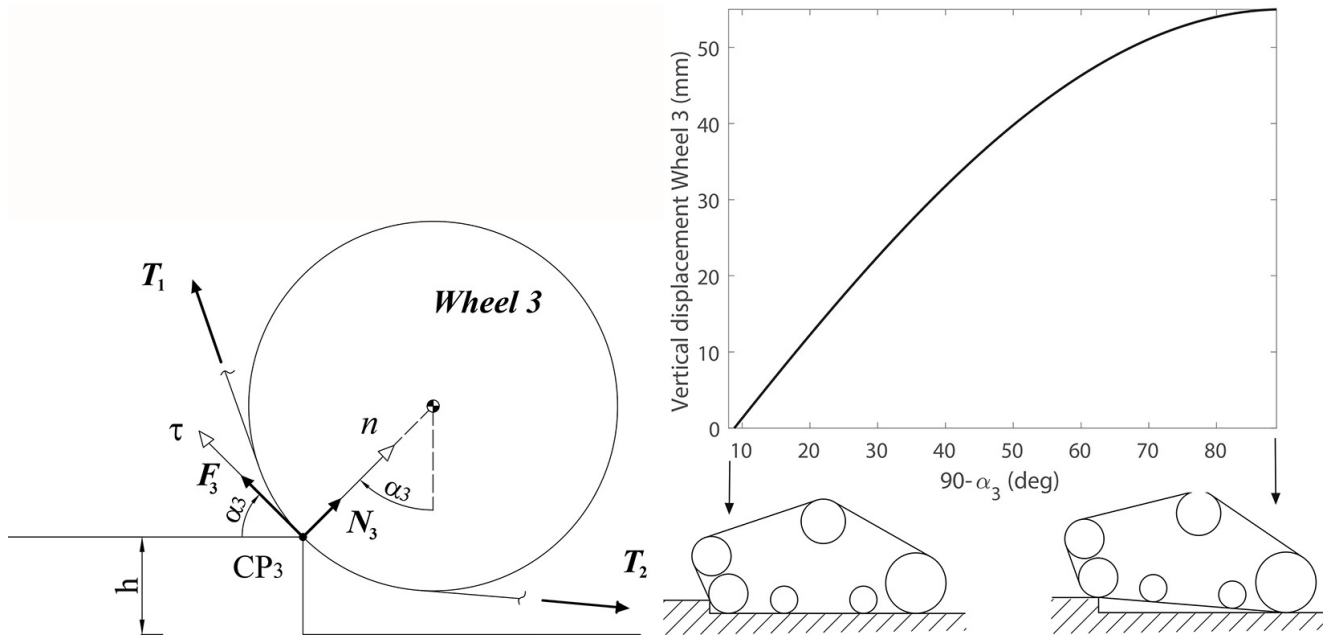


Fig. 3: Single wheel contact model: (left) Free-body diagram of Wheel 3, (right) vertical displacement of Wheel 3 as a function of its contact angle α_3

66 where f_c are the wheel-ground interaction forces, f_{int} the internal forces (i.e. track tensions and spring forces), and f_s the
 67 summed effect of gravitational and external forces. G_c and G_{int} are functions of the seven degrees of freedom of the robot.
 68 Overall, Eq. (2) results in a system of 24 equations in 24 unknowns. Details are reported in Appendix A. Note that the force
 69 distribution equation (2) has been extended with respect to [16] to include the change in track tension at each contact point.
 70 Given the geometry and inertial properties of the robot and the position of the wheel contact points CP_i and the corresponding
 71 contact angles α_i , Eq. (2) predicts the robot configuration and the wheel-ground forces (upper part of Fig. 4) and internal
 72 forces (lower part of Fig. 4) acting on the system.

73 When a standard tracked robot is considered, wheels are attached to the chassis. Therefore, as soon as Wheel 3 starts climbing
 74 the obstacle, Wheels 4 and 5 lift and the only contact forces are those acting on the first and last wheel. The behaviour of a
 75 standard robot can be obtained from Eq. (2) by removing the null unknowns and the corresponding rows and columns.

76 3.1.1 Virtual work

77 The principle of virtual displacements is a powerful method for the dynamic analysis of multibody systems using an
 78 energetic approach. In the case of Polibot it can be defined as

$$\delta W = \delta L_{mot} + \delta L_g + \delta L_{el} + \delta L_{slip} = 0 \quad (3)$$

79 meaning that the virtual work of all forces δW acting on the system must be zero. δL_{mot} is the virtual work of the drive torque,
 80 δL_g that of the gravitational forces, δL_{el} that of the elastic forces of the suspension system, and δL_{slip} the work associated
 81 with the longitudinal slip of the ground wheels. Expressions of the single virtual works are given in Appendix B. Equation
 82 (3) will be used to obtain the different energy contributions in terms of gravitational, elastic and slip components.

83 4 Results

84 The behavior of Polibot is compared with that of an analog vehicle that employs a standard fixed-wheel configuration.
 85 Two test cases are considered: the traverse of a step-like obstacle and the upward navigation of a vertical surface. The
 86 behavior of the two robots is evaluated based on the following metrics:

87 Minimum friction coefficient: the smaller the required friction, the better the climbing ability.

88 Drive motor torque: the higher the torque, the bigger the size of the drive motor, which is bulkier and adds more weight
 89 to the robot.

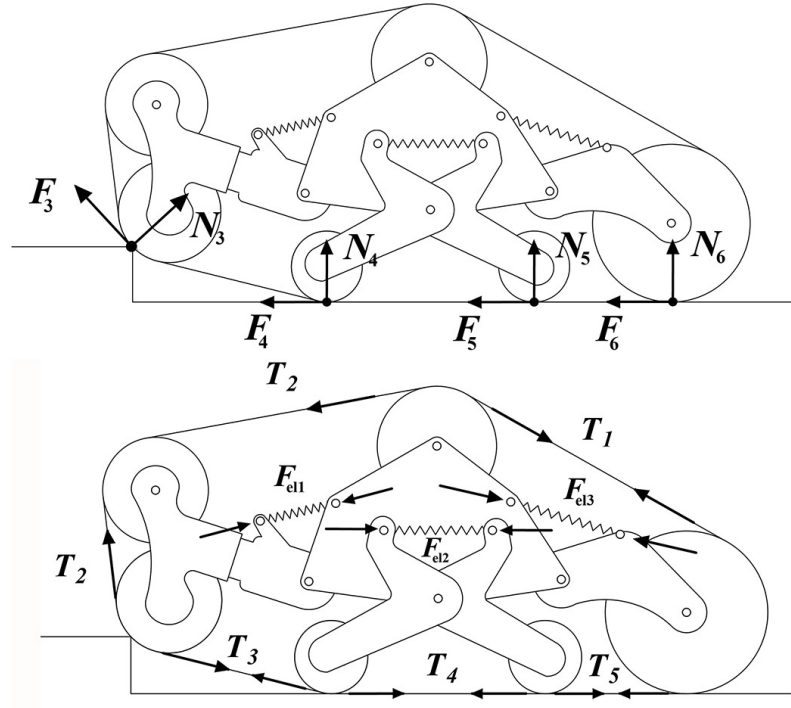


Fig. 4: Force systems acting on the robot: (top) contact forces $[F_i, N_i]^T$ that each of the four wheels exchange with the ground, (bottom) internal forces including track tensions T_i and spring forces $F_{el,i}$ in the suspension system

90 Ground pressure distribution: the more uniformly distributed the normal pressure under the track, the better the tractive
 91 performance of the vehicle [19].

92 4.1 Obstacle traverse

93 The worst-case condition of wheel contact is considered where Wheels 2 and 3 lift, whereas Wheels 4 onward remain
 94 in contact with flat ground, as shown in Fig. 2 (top). The obstacle height is set as about 85% of the wheel radius ($h/R=0.8$,
 95 $h=0.055$ mm, $R=0.065$ mm). The minimum coefficient of friction required by Polibot and its fixed-wheel counterpart is
 96 plotted in Fig. 5 as a function of the vertical displacement of Wheel 3. The starting phase of the climbing manouver is the
 97 most critical. The value of the minimum coefficient of friction required by Polibot is 0.45, whereas that of the fixed-wheel
 98 robot almost doubles ($=0.83$). During the climbing stage, the required friction decreases as Polibot confirms its superiority
 99 over the robot without a suspension system. A similar result is achieved when looking at the torque drawn by the drive motor
 100 that controls the track sprocket, as shown in Fig. 6. Polibot's required torque is significantly lower than that of the standard
 101 robot. The maximum request results in 0.74 and 1.21 Nm, respectively, for the suspended and rigid robot.

102 The use of a passive suspension promotes a more uniform ground pressure beneath the tracks. During obstacle crossing,
 103 all wheels remain in contact with the ground, guaranteeing a better load distribution between the wheels and the ground,
 104 thus reducing the minimum friction coefficient. In the case of a rigid robot, as soon as Wheel 3 starts climbing the obstacle,
 105 wheels 4 and 5 lose contact. Consequently, load peaks are observed under wheels 3 and 6. A normalized deviation of the
 106 normal force acting on the wheels can be introduced as

$$\sigma_N = \frac{\sqrt{\frac{1}{4} \sum_{i=3}^6 (N_i - \bar{N})^2}}{\bar{N}} \quad (4)$$

107 with:

$$\bar{N} = \frac{1}{4} \sum_{i=1}^4 N_i \quad (5)$$

108 where N_i ($i = 3, \dots, 6$) is the normal force acting on the i -th ground wheel. The lower σ_N , the more uniform the ground

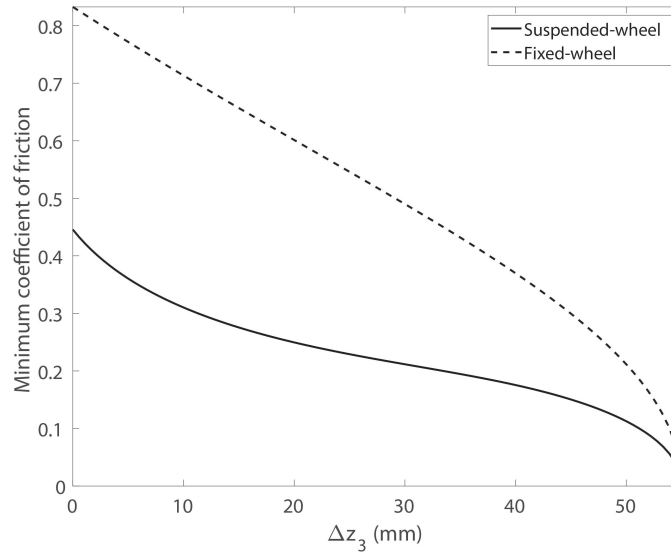


Fig. 5: Minimum coefficient of friction expressed as a function of the front wheel vertical displacement.

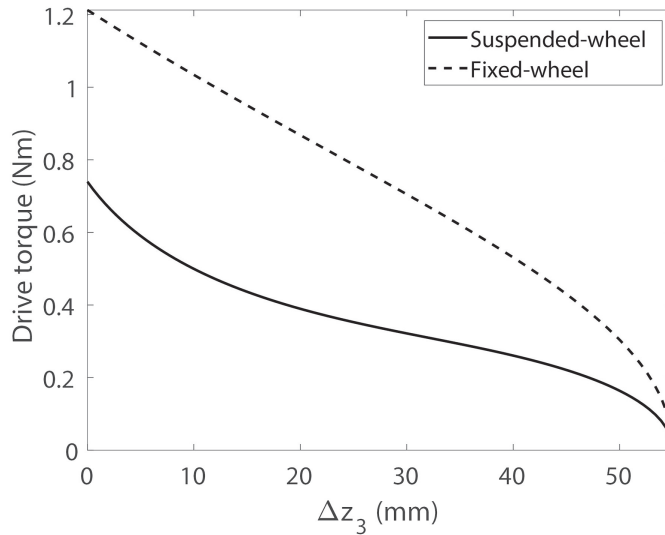


Fig. 6: Required drive torque expressed as a function of the front wheel vertical displacement

109 pressure distribution resulting in improved traction ability and reduced soil compaction. Figure 7 compares σ_N as obtained
 110 from the Polibot and its fixed-wheel counterpart during the step-like obstacle crossing. As seen from this figure, adopting
 111 the suspension system ensures a better ground pressure distribution during the entire maneuver.

112 4.1.1 Energy balance

113 It is interesting to evaluate the different contributions to the drive effort during the obstacle crossing manoeuvre using the
 114 principle of virtual work, as explained in Section 3.1.1 and Appendix B. First, the standard fixed-wheel Polibot is analyzed
 115 and the results are shown in the left plot of Figure 8. The energy delivered by the drive motor (black solid line) balances
 116 partly the increase in the gravitational potential energy due to the lift of the robot (grey solid line) and partly the energy
 117 loss (black dashed line) due to slippage of Wheel 6. The energy balance for the suspended Polibot is shown in right plot of
 118 Figure 8. In the initial stage of the climbing maneuver, the suspension system tends to contract and store elastic potential
 119 energy (black dotted line). In this phase, the robot center of mass slightly lowers, thus explaining the negative contribution
 120 of the gravitational component (grey solid line). The elastic energy is partially returned to the system in the second part of
 121 the maneuver contrasting the increase in the gravitational energy. Compared with the rigid robot, the slippage loss (black
 122 dashed line) is larger in the first part (up to $\Delta z_3 = 20mm$) and smaller in the second part. The advantage of adopting a passive

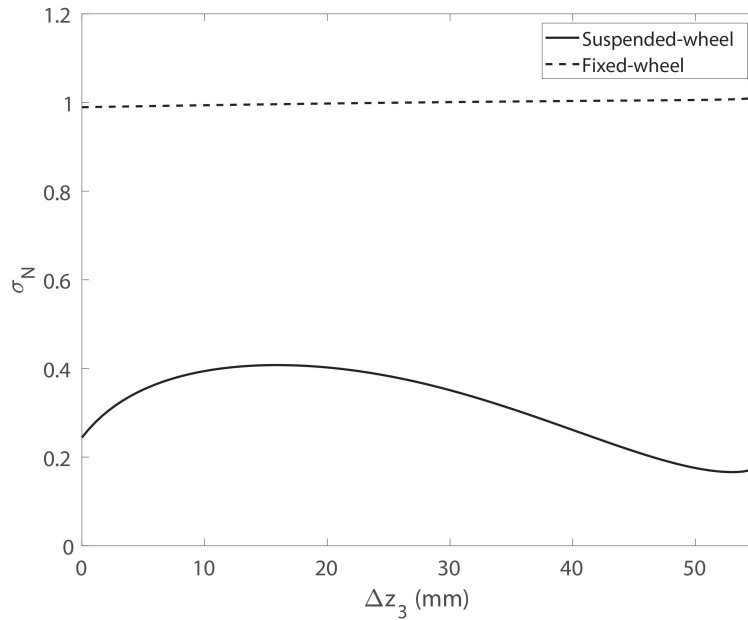


Fig. 7: Normalized deviation of the ground normal force as a function of the front wheel vertical displacement

123 articulated suspension system appears double-fold. On the one hand, obstacle crossing is achieved with a more progressive
 124 lift of the robot center of mass, resulting in a significant decrease of energy peak. On the other hand, the ability to store and
 release elastic potential energy serves as a buffer that can be helpful to cover energy requests.

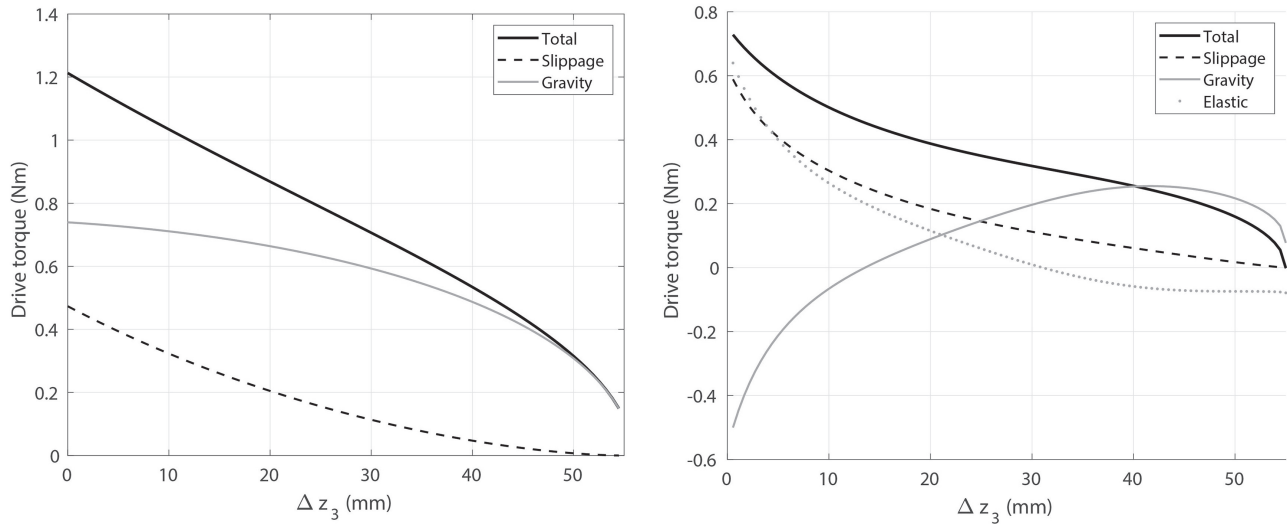


Fig. 8: Total drive torque divided in its gravitational and slippage component: rigid robot (left), Polibot (right)

125

126 4.2 Wall negotiation

127 The climbing of a vertical surface represents a limit case, where the obstacle is infinitely tall, as shown in Figure 9. In
 128 terms of obstacle climbing ability, it refers to practical scenarios where an obstacle has a height greater than the radius of the
 129 front wheel. It is assumed that the friction coefficient between the track and the wall is known ($=0.7$) and constant during
 130 the maneuver. The idler Wheel 2 gets in contact with the wall and starts climbing, resulting in the lift of Wheel 3, in the
 131 case of the suspended Polibot, and the wheels 3, 4 and 5 in the case of the rigid robot. When comparing the two vehicles
 132 in terms of minimum coefficient of friction with the ground, the adoption of the suspension system ensures a reduction of
 133 58% compared to the rigid chassis (0.33 versus 0.78), as shown in Figure 10(top). Better performance is also achieved in the

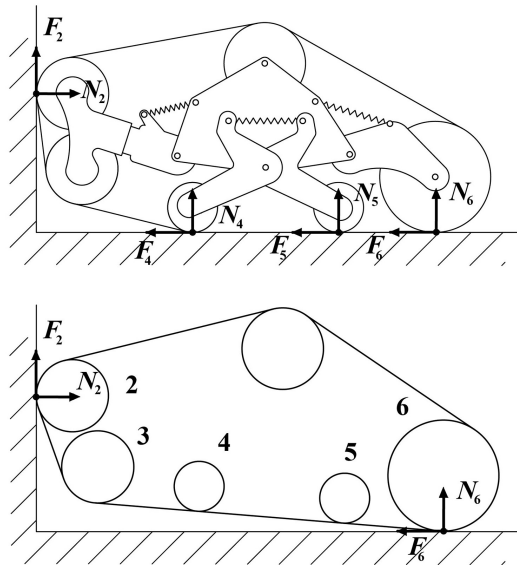


Fig. 9: Wall climbing in the case of the suspended Polibot (top) and rigid robot (bottom).

134 maximum drive torque (Figure 10, middle) and normalized deviation of the normal force σ_N (Figure 10, bottom).

135 4.2.1 Energy balance

136 Similarly to the case of the step-like obstacle, the different contributions to the drive effort are investigated using the
 137 principle of virtual work. The results are shown in Figure 11 for the rigid (left) and the suspended Polibot (right). The
 138 compliance provided by the suspension system reduces the overall energy request. The robot center of mass is lifted more
 139 gradually, resulting in a significant decrease in the gravitational energy request (grey solid line). The loss due to slippage
 140 (black dashed line) is also lower as the wheel displacements can be accommodated more easily. One additional advantage is
 141 that the energy spent to load the elastic elements of the suspension (black dotted line) is stored (not dissipated) and can be
 142 returned to the system.

143 5 Experimental validation

144 Experiments are performed with the all-terrain robot Polibot (see Fig. 1). In nominal mode, the vehicle uses its passive
 145 suspension system, as explained in Section 2. By replacing the spring-damper elements with steel rods, Polibot can operate
 146 in fixed-wheel mode instead. Two sets of experiments are performed that replicate the scenarios previously solved via the
 147 analytical model, namely, the traverse of an obstacle of 55 mm height and the negotiation of a vertical wall, as shown in Fig.
 148 12. Both types of obstacles are tackled simultaneously by the two tracks to avoid asymmetries. The travel velocity of the
 149 robot is set as 0.05 m/s to comply as much as possible with the underlying quasi-static assumption. During the experiments,
 150 the sprocket rotations and the electrical current drawn by the drive motor are recorded. The relationship between the sprocket
 151 rotation and the corresponding vertical displacement is obtained from Eq. (1). For brushed motors, the drive torque can be
 152 indirectly measured through a linear relationship with the electrical current [20]. Each test has been repeated five times and
 153 the average values are shown in Fig. 13. The motor current drawn by the drive motors of Polibot operating in nominal mode
 154 (fixed-wheel) is marked by a solid (dashed) black line. It should be noted that for a fair comparison with the results obtained
 155 via the analytical model the component of the electrical current related with the motion resistance has been subtracted
 156 from the total electrical current. The contribution of motion resistance due to internal friction and interaction with the
 157 ground has been obtained by performing straight motion tests at constant speed. As seen in Fig. 13, for both scenarios of
 158 single obstacle traverse (a) and wall negotiation (b), Polibot requires less torque when operating in the nominal suspended
 159 configuration than in the fixed-wheel mode. The average decrease in drive effort is about 30% in the case of obstacle traverse
 160 and about 50% in the case of wall climbing. The experimental driving torque profiles of Figure 13 can be compared with the
 161 theoretical counterparts obtained for the traverse of a single obstacle and the navigation upward along a vertical surface, as
 162 shown in Figure 6 and Figure 10, respectively. It can be observed that the agreement is good enough showing consistency
 163 between experiments and theory. Discrepancies can be expected as the analytical model neglects various effects including
 164 the efficiency of the transmission driveline. In addition, it should be noted that the analytical driving torque profile is based
 165 on numerical optimization to solve the non-linear problem expressed by Equation (2) under simplifying assumption, e.g.
 166 minimum coefficient of friction (Refer to Section 4.1). Similar conditions cannot be replicated in real experiments.

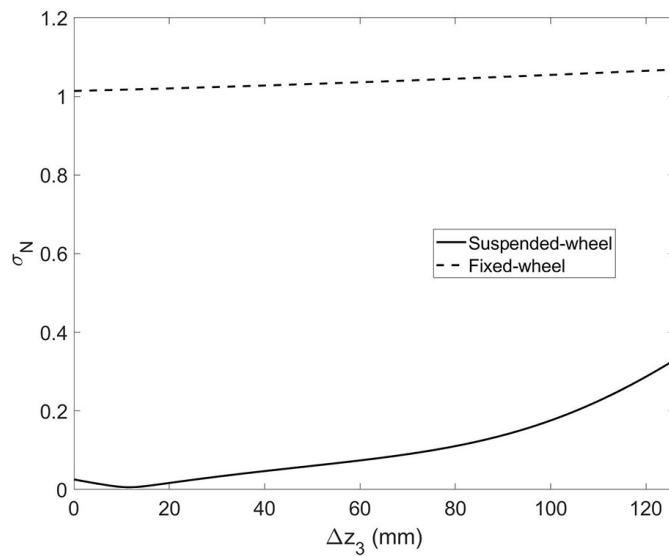
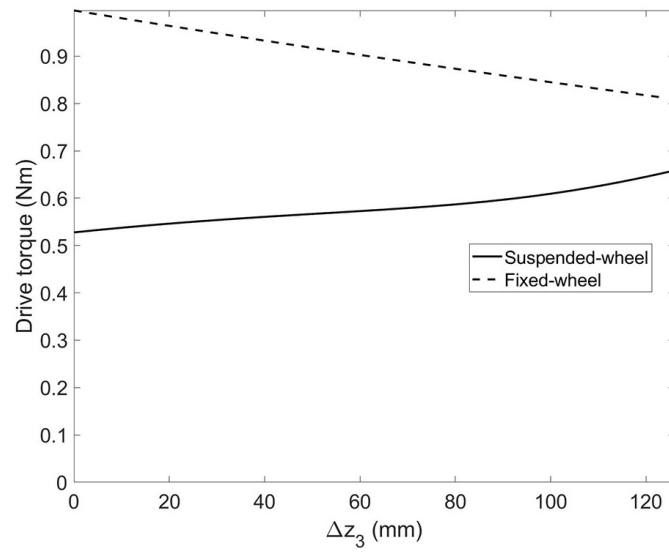
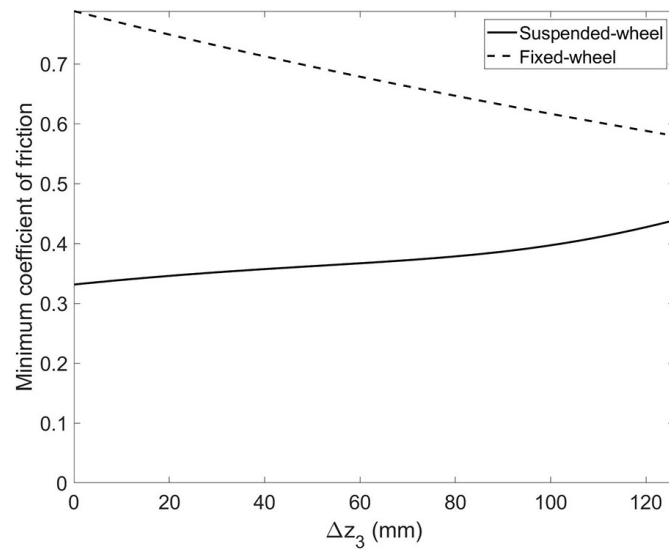


Fig. 10: Wall climbing. Comparison of Polibot with a rigid robot: (top) minimum coefficient of friction, (middle) drive torque, (bottom) normalized deviation of the normal force.

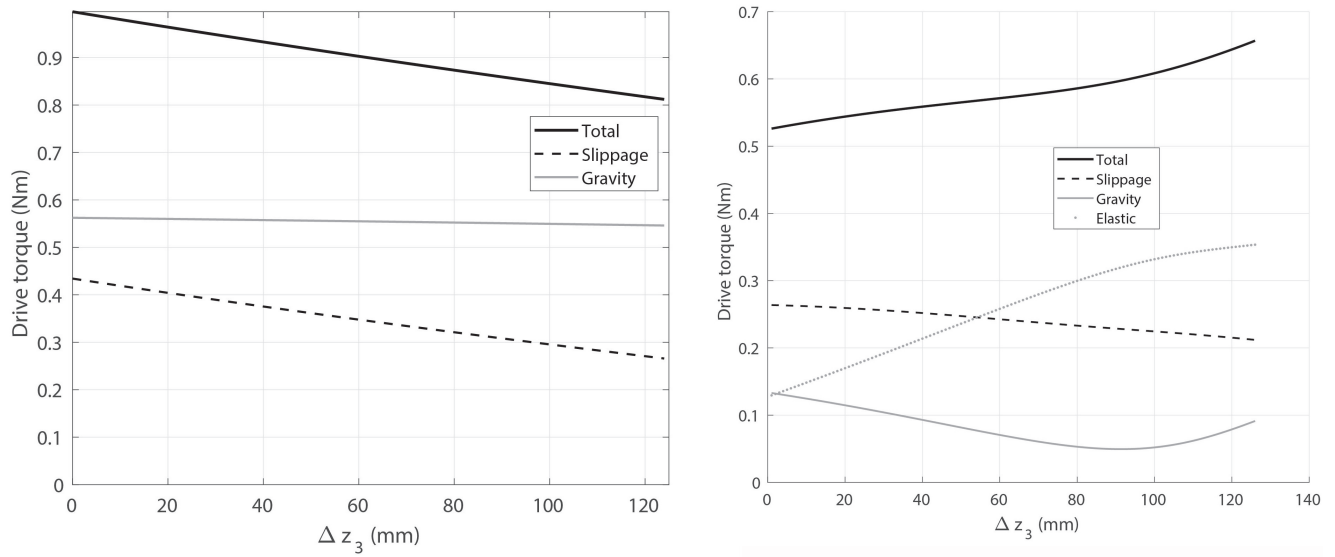


Fig. 11: Total drive torque divided in its slippage, gravitational and elastic component: rigid Polibot (left), suspended Polibot (right)



Fig. 12: Experimental validation using the tracked robot Polibot: obstacle traverse (top), upward wall navigation (bottom)

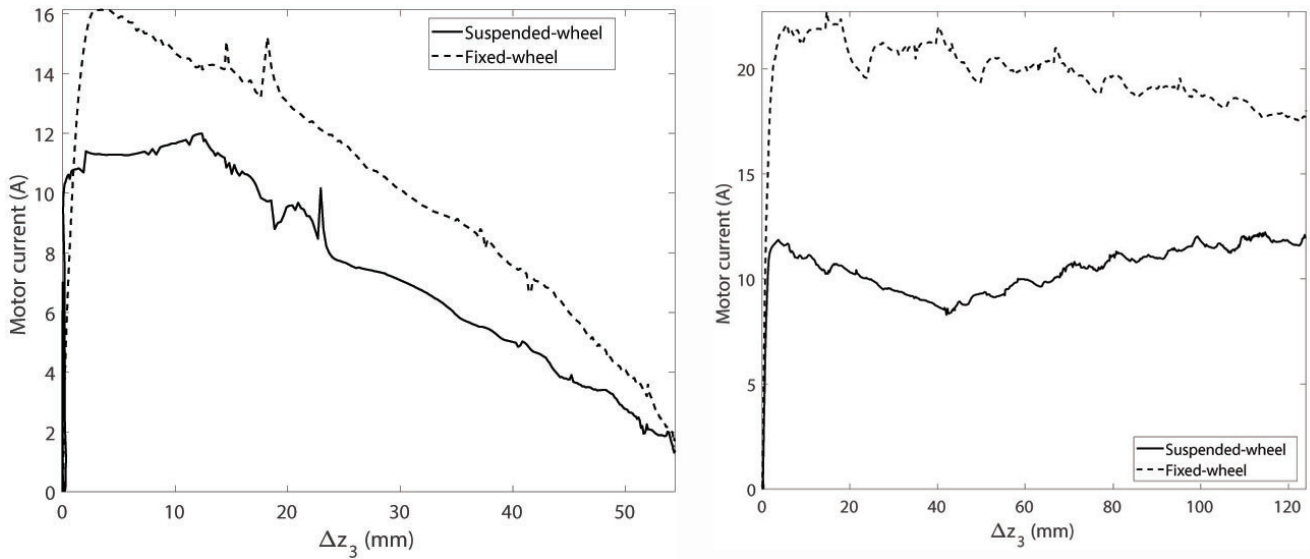


Fig. 13: Experimental results obtained from Polibot operating in suspended and fixed-wheel configuration. Electrical current drawn by the drive motors: (left) obstacle traverse, (right) wall negotiation

6 Conclusions

167

168 The paper presented an in-depth investigation of the climbing ability of a novel tracked robot that adopts a passively articulated suspension system. Based on a quasi-static Newton-Euler model, it was shown that Polibot outperforms a standard tracked analog with a fixed-wheel layout in the traverse of a step-like obstacle and in the climb of a vertical wall. The reduction in the required minimum friction coefficient and the maximum drive effort resulted, respectively, in 46% (58%) and 39% (48%) for the single obstacle case (wall negotiation). A significant more uniform ground pressure distribution was also observed. By applying the principle of virtual work, it was possible to obtain the energy balance of the system and evaluate the contribution of the different forces involved. One advantage of the adoption of a passive suspension system is that the elastic potential energy can be stored in the system and released to cover energy peaks. The possibility to accommodate wheel displacements is also positive to reduce energy loss caused by track slippage, especially in the wall climbing.

173
174
175
176
177
178 Parallel to the theoretical study, an experimental activity has been developed to validate the analytical findings using the real Polibot prototype that was appropriately instrumented and tested. The experimental results demonstrated the validity of the proposed approach. Future directions of the research will focus on the model-based optimization of the suspension geometry and elastic stiffness to maximize the climbing ability of the robot. In addition, by monitoring the torque delivered by the tracks it may be possible to develop strategies for adaptive control of the robot during obstacle negotiation. The availability of potentiometers to measure the relative rotations of the various components of the suspension system may also enable the reconstruction of obstacle geometry and terrain topography in general based on the quasi-static kinematic model.

Acknowledgments

185

186 The financial support of the projects: giving Smell sense To Agricultural Robotics (STAR), ERA-NET COFUND ICT AGRI-FOOD (Grant No. 45207), and AgRibot - Harnessing Robotics, XR/AR, and 5G for a New Era of Safe, Sustainable, and Smart Agriculture, European Union's Horizon Europe research and innovation programme under grant agreement (No. 101183158), are gratefully acknowledged. This work was also partially supported by the projects: Programme "Department of Excellence" Legge 232/2016 (Grant No. CUP - D93C23000100001), funded by the Italian Ministry of University and Research, and NODES, which has received funding from the MUR - M4C2 1.5 of PNRR funded by the European Union - NextGenerationEU (Grant agreement no. ECS00000036).

Appendix

193

A Force distribution equation

194

195 Equation (2) expresses the quasi-static equilibrium equations of the Polibot half-symmetry model. The expression of the single terms in Eq. (2) can be obtained by applying the Newton-Euler equations to the whole system and the single suspension swing arms. The motion resistance, F_v , accounts for the internal resistance of the running gear and the resistance due to interaction with the terrain. Please, refer to Fig. A.1 for the meaning of the geometric parameters involved. More

198

199 details on the assembly of Eq. (2) and its solution can be found in [16]. Note that $c(\cdot)$ and $s(\cdot)$ stand for $\cos(\cdot)$ and $\sin(\cdot)$,
 200 respectively.

$$f_c = \begin{bmatrix} F_3 \\ N_3 \\ F_4 \\ N_4 \\ F_5 \\ N_5 \\ F_6 \\ N_6 \end{bmatrix}; f_{est} = \begin{bmatrix} T_1 \\ T_2 \\ T_3 \\ T_4 \\ T_5 \\ F_{el,1} \\ F_{el,2} \\ F_{el,3} \end{bmatrix}; f_s = \begin{bmatrix} F_v \\ W \\ 0 \\ 0 \\ 0 \\ 0 \\ 0 \\ 0 \\ 0 \\ 0 \\ 0 \\ 0 \\ 0 \\ 0 \\ 0 \end{bmatrix}; \quad (A.1)$$

201

$$G_c = \begin{bmatrix} c\alpha_3 & -s\alpha_3 & 1 & 0 & 1 & 0 & 1 & 0 \\ s\alpha_3 & c\alpha_3 & 0 & 1 & 0 & 1 & 0 & 1 \\ s\alpha_3(X_P - X_G) & c\alpha_3(X_P - X_G) & -h & X_K - X_G & -h & X_I - X_G & -h & X_M - X_G \\ s\alpha_3(X_D - CP_3^x) + c\alpha_3(X_D - CP_3^y) + c\alpha_3(Z_D - CP_3^z) & -s\alpha_3(Z_D - CP_3^z) & 0 & 0 & 0 & 0 & 0 & 0 \\ 0 & 0 & Z_F - CP_4^z & X_F - X_K & 0 & 0 & 0 & 0 \\ 0 & 0 & 0 & 0 & -(Z_F - CP_5^z) & X_I - X_F & 0 & 0 \\ 0 & 0 & 0 & 0 & 0 & 0 & -(Z_E - CP_6^z) & X_M - X_E \\ 1 & 1 & 1 & 1 & 0 & 0 & 0 & 0 \\ -1 & 0 & 0 & 0 & 0 & 0 & 0 & 0 \\ 0 & 0 & -1 & 0 & 0 & 0 & 0 & 0 \\ 0 & 0 & 0 & 0 & -1 & 0 & 0 & 0 \\ 1 & -k_c & 0 & 0 & 0 & 0 & 0 & 0 \\ 0 & 0 & 1 & -k_c & 0 & 0 & 0 & 0 \\ 0 & 0 & 0 & 0 & 1 & -k_c & 0 & 0 \\ 0 & 0 & 0 & 0 & 0 & 0 & 1 & -k_c \end{bmatrix} \quad (A.2)$$

202

$$G_{int} = \begin{bmatrix} 0 & 0 & 0 & 0 & 0 & 0 & 0 & 0 \\ 0 & 0 & 0 & 0 & 0 & 0 & 0 & 0 \\ 0 & 0 & 0 & 0 & 0 & 0 & 0 & 0 \\ 0 & a & -b & 0 & 0 & 0 & 0 & -g \\ 0 & 0 & c & -(Z_F - CP_4^z) & 0 & -e & 0 & 0 \\ 0 & 0 & 0 & -(Z_F - CP_5^z) & (Z_F - CP_5^z) & -e & 0 & 0 \\ d & 0 & 0 & 0 & -(Z_E - CP_5^z) & 0 & -f & 0 \\ -1 & 1 & 0 & 0 & 0 & 0 & 0 & 0 \\ 0 & -1 & 1 & 0 & 0 & 0 & 0 & 0 \\ 0 & 0 & -1 & 1 & 0 & 0 & 0 & 0 \\ 0 & 0 & 0 & -1 & 1 & 0 & 0 & 0 \\ 0 & 0 & 0 & 0 & 0 & 0 & 0 & 0 \\ 0 & 0 & 0 & 0 & 0 & 0 & 0 & 0 \\ 0 & 0 & 0 & 0 & 0 & 0 & 0 & 0 \\ 0 & 0 & 0 & 0 & 0 & 0 & 0 & 0 \end{bmatrix}; \quad (A.3)$$

203 B Virtual work

204 The virtual work of the drive motor torque C_m can be obtained as

$$\delta L_{mot} = C_m \delta \theta_1^{rel} \tau \quad (B.4)$$

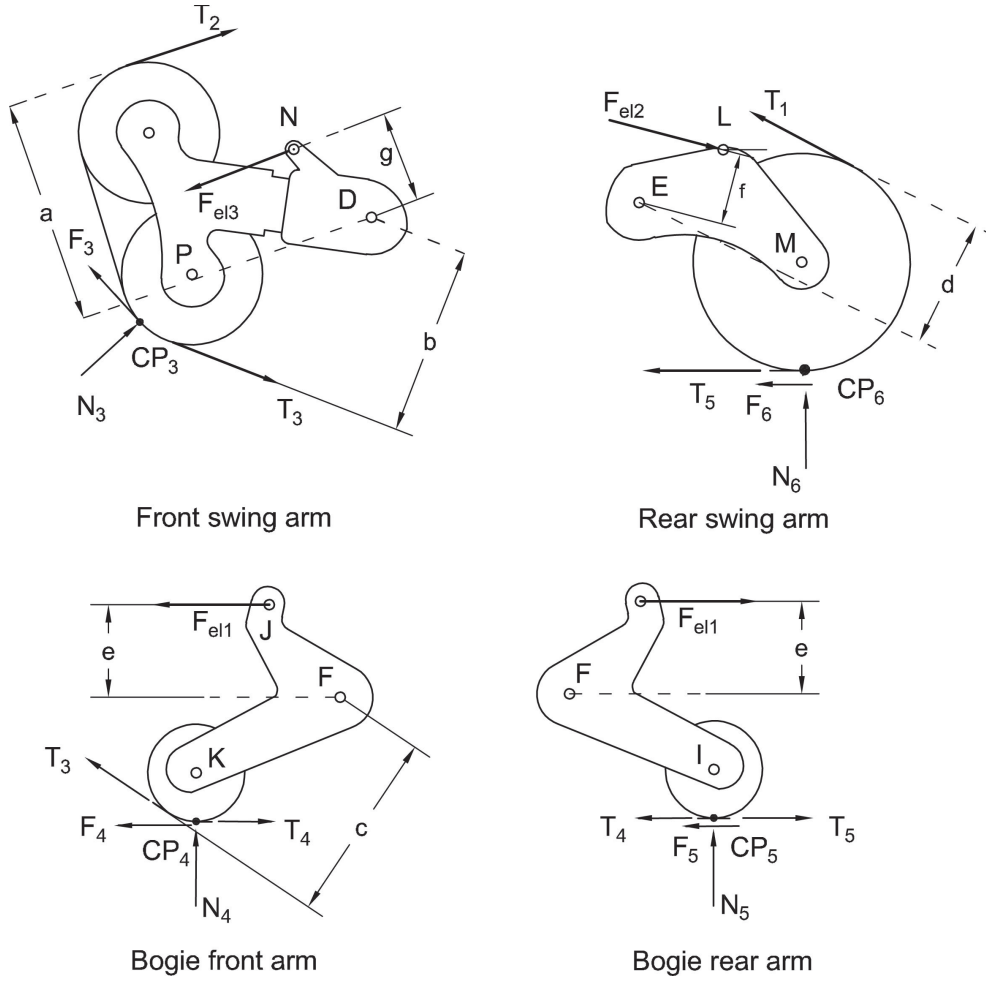


Fig. A.1: Individual free-body diagrams of the four suspension swing arms

205 where $\delta\theta_1^{rel}$ is the virtual rotation of the sprocket relative to the chassis, and $\tau(=30)$ the transmission ratio. The virtual work
 206 of the weight force W is

$$\delta L_g = W\delta z_G \quad (B.5)$$

207 where δz_G is the virtual vertical displacement of the robot center of mass. The virtual elastic work δL_{el} is given by the sum
 208 of the contribution of the three spring elements. For the i -th elastic force $F_{el,i}$, one gets

$$\delta L_{el,i} = F_{el,i}\delta l_i \quad (B.6)$$

209 being δl_i the deformation of the i -th spring element. Please note that the elastic virtual work δL_{el} applies only to the suspended
 210 Polibot, while it is null for the fixed-wheel robot. A special treatment deserves the virtual work lost in the wheel-ground
 211 interaction due to slippage. Assuming a pure rolling condition for Wheel 3 that crosses the obstacle, the other wheels will
 212 necessarily undergo slippage to comply with the kinematic constraints of the system. To better explain the problem, the case
 213 of the fixed-wheel robot is considered. Figure B.2 shows the virtual displacement field for the rigid Polibot consistent with
 214 its boundary and constraint conditions. The vehicle rotates $\delta\theta$ around its instantaneous center of rotation K , which can be
 215 found by intersecting the two normal directions of contact, n_3 and n_6 , at wheels 3 and 6, respectively. As a result, points P
 216 and M experience virtual displacements $\delta P = \delta\theta\overline{KP}$ and $\delta M = \delta\theta\overline{KM}$. Wheel 3 is assumed to roll of $\delta\theta_3 = \delta P/R_3$, R_3 being
 217 the wheel radius. With respect to the robot chassis, the relative displacement of Wheel 3 is $\delta\theta_3^{rel} = \delta\theta_3 - \delta\theta$. By considering
 218 the track coupling between wheels 3 and 6, the relative displacement of Wheel 6 can be obtained as $\delta\theta_6^{rel} = \delta\theta_3^{rel}R_3/R_6$, and
 219 finally $\delta\theta_6 = \delta\theta_6^{rel} + \delta\theta$.

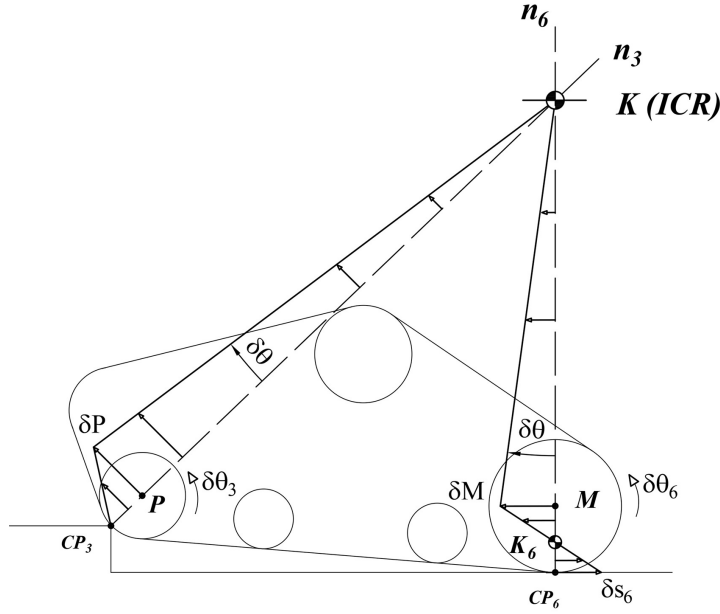


Fig. B.2: Virtual displacement field for the fixed-wheel Polibot

220 The instantaneous center of rotation of Wheel 6 can be found as

$$\overline{K_2M} = \frac{\delta M}{\delta \theta_6} \quad (\text{B.7})$$

221 and the corresponding slippage at contact point CP_6

$$\delta s_6 = \delta \theta_6 (R_6 - \overline{K_6M}) \quad (\text{B.8})$$

222 Then, the virtual work dissipated in the slippage of Wheel 6 is

$$\delta L_s = F_6 \delta s_6 \quad (\text{B.9})$$

223 A similar approach can be followed for the suspended Polibot to obtain the virtual work due to slippage incurred by wheels
 224 4, 5, and 6. The relative virtual displacement of the wheels with respect to the chassis is provided as output by the multi-body
 225 model of Polibot expressed by Equation (2).

226 In summary, by applying the principle of virtual work (3), it is possible to obtain an alternate expression for the drive torque
 227 following an energetic approach. For the fixed-wheel Polibot, one gets

$$C_m^{fix} = \frac{\delta L_g}{\delta \theta_1^{rel} \tau} + \frac{\delta L_s}{\delta \theta_1^{rel} \tau} \quad (\text{B.10})$$

228 In the case of the suspended Polibot, it leads to

$$C_m^{susp} = \frac{\delta L_g}{\delta \theta_1^{rel} \tau} + \frac{\delta L_s^{susp}}{\delta \theta_1^{rel} \tau} + \frac{\delta L_{el}}{\delta \theta_1^{rel} \tau} \quad (\text{B.11})$$

229 where $\delta L_s^{susp} = \delta L_{s,4} + \delta L_{s,5} + \delta L_{s,6}$.

References

- [1] Ugenti, A., Vulpi, F., Domínguez, R., Cordes, F., Milella, A., and Reina, G., 2022. “On the role of feature and signal selection for terrain learning in planetary exploration robots”. *Journal of Field Robotics*, **39**(4), pp. 355–370.
- [2] Leanza, A., Galati, R., Ugenti, A., Cavallo, E., and Reina, G., 2023. “Where am I heading? a robust approach for orientation estimation of autonomous agricultural robots”. *Computers and Electronics in Agriculture*, **210**, p. 107888.
- [3] Choi, Y., Jeong, K., Seo, Y., uk Lee, S., Cho, J., Jung, S., and Kim, S., 2008. “QuadTrack-II: A remotely operated mobile robot with four articulated tracks”. *IFAC Proceedings Volumes*, **41**(2), pp. 3017–3020. 17th IFAC World Congress.
- [4] Galati, R., Mantriota, G., and Reina, G., 2021. “Design and development of a tracked robot to increase bulk density of flax fibers”. *Journal of Mechanisms and Robotics*, **13**(5).
- [5] Demirjian, W., Powelson, M., and Canfield, S., 2020. “Design of Track-Type Climbing Robots Using Dry Adhesives and Compliant Suspension for Scalable Payloads”. *Journal of Mechanisms and Robotics*, **12**(3), 02, p. 031017.
- [6] Shafaei, S., and Mousazadeh, H., 2023. “Experimental comparison of locomotion system performance of ground mobile robots in agricultural drawbar works”. *Smart Agricultural Technology*, **3**, p. 100131.
- [7] Wong, J., and Huang, W., 2006. “Wheels vs. tracks”—a fundamental evaluation from the traction perspective”. *Journal of Terramechanics*, **43**, 04, p. 27–42.
- [8] Bruzzone, L., Nodehi, S. E., and Fanghella, P., 2022. “Tracked locomotion systems for ground mobile robots: A review”. *Machines*, **10**(8), p. 648.
- [9] Lewis, P. J., Flann, N., Torrie, M. R., Poulson, E. A., Petroff, T., and Witus, G., 2005. “Chaos, an intelligent ultra-mobile SUGV: combining the mobility of wheels, tracks, and legs”. In *Unmanned Ground Vehicle Technology VII*, G. R. Gerhart, C. M. Shoemaker, and D. W. Gage, eds., Vol. 5804, International Society for Optics and Photonics, SPIE, pp. 427 – 438.
- [10] Yajima, R., and Nagatani, K., 2021. “Obstacle climbing of tracked robot for unfixed cylindrical obstacle using sub-tracks”. In *Field and Service Robotics*, G. Ishigami and K. Yoshida, eds., Springer Singapore, pp. 189–203.
- [11] Brunner, M., Fiolka, T., Schulz, D., and Schlick, C. M., 2015. “Design and comparative evaluation of an iterative contact point estimation method for static stability estimation of mobile actively reconfigurable robots”. *Robotics Auton. Syst.*, **63**, pp. 89–107.
- [12] Szpaczyńska, D., Łopatka, M., and Krogul, P., 2024. “The running gear construction impact on overcoming obstacles by light high-mobility tracked ugv”. *Journal of Terramechanics*, **112**, pp. 1–17.
- [13] Kim, J., Kim, J., and Lee, D., 2018. “Mobile robot with passively articulated driving tracks for high terrainability and maneuverability on unstructured rough terrain: Design, analysis, and performance evaluation”. *Journal of Mechanical Science and Technology*, **32**(11), pp. 5389–5400.
- [14] Sun, B., and Jing, X., 2017. “A tracked robot with novel bio-inspired passive ”legs””. *Robotics and biomimetics*, **4**(1), pp. 1–14.
- [15] Benamar, F., and Grand, C., 2013. “Quasi-Static Motion Simulation and Slip Prediction of Articulated Planetary Rovers Using a Kinematic Approach”. *Journal of Mechanisms and Robotics*, **5**(2), 03, p. 021002.
- [16] Ugenti, A., Galati, R., Mantriota, G., and Reina, G., 2023. “Analysis of an all-terrain tracked robot with innovative suspension system”. *Mechanism and Machine Theory*, **182**, p. 105237.
- [17] Grazioso, A., Ugenti, A., Galati, R., Mantriota, G., and Reina, G., 2023. “Modeling and validation of a novel tracked robot via multibody dynamics”. *Robotica*, **41**(10), p. 3211–3232.
- [18] Reina, G., and Foglia, M., 2013. “On the mobility of all-terrain rovers”. *Industrial Robot: An International Journal*, **40**(2), pp. 121–131.
- [19] Wong, J. Y., 2008. *Theory of ground vehicles*. John Wiley & Sons.
- [20] Reina, G., and Galati, R., 2016. “Slip-based terrain estimation with a skid-steer vehicle”. *Vehicle System Dynamics*, **54**(10), p. 1384 – 1404.